Journal of Magnetic Resonance 307 (2019) 106573

Contents lists available at ScienceDirect

Journal of Magnetic Resonance

journal homepage: www.elsevier.com/locate/jmr

Modular, triple-resonance, transmission line DNP MAS probe for 500 MHz/330 GHz

Marcel Reese [a], Christy George [a], Chen Yang [a], Sudheer Jawla [b], J. Tassilo Grün [d], Harald Schwalbe [d], Christina Redfield [e], Richard J. Temkin [b,c], Robert G. Griffin [a,*]

[a] *Department of Chemistry and Francis Bitter Magnet Laboratory, Massachusetts Institute of Technology, Cambridge, MA 02139, United States*
[b] *Plasma Science and Fusion Center, Massachusetts Institute of Technology, Cambridge, MA 02139, United States*
[c] *Department of Physics, Massachusetts Institute of Technology, Cambridge, MA 02139, United States*
[d] *Institute for Organic Chemistry and Chemical Biology, Center for Biomolecular Magnetic Resonance, Johann Wolfgang Goethe-Universität Frankfurt, 60438 Frankfurt, Germany*
[e] *Department of Biochemistry, University of Oxford, South Parks Road, Oxford OX1 3QU, United Kingdom*

ARTICLE INFO

Article history:
Received 3 July 2019
Revised 12 August 2019
Accepted 13 August 2019
Available online 14 August 2019

Keywords:
Solid state DNP
Balanced transmission line probe
NMR probe characterization
Novel probe design

ABSTRACT

We describe the design and construction of a modular, triple-resonance, fully balanced, DNP-MAS probe based on transmission line technology and its integration into a 500 MHz/330 GHz DNP-NMR spectrometer. A novel quantitative probe design and characterization strategy is developed and employed to achieve optimal sensitivity, RF homogeneity and excellent isolation between channels. The resulting three channel HCN probe has a modular design with each individual, swappable module being equipped with connectorized, transmission line ports. This strategy permits attachment of a mating connector that facilitates accurate impedance measurements at these ports and allows characterization and adjustment (e.g. for balancing or tuning/matching) of each component individually. The RF performance of the probe is excellent; for example, the ^{13}C channel attains a Rabi frequency of 280 kHz for a 3.2 mm rotor. In addition, a frequency tunable 330 GHz gyrotron operating at the second harmonic of the electron cyclotron frequency was developed for DNP applications. Careful alignment of the corrugated waveguide led to minimal loss of the microwave power, and an enhancement factor $\varepsilon = 180$ was achieved for U-^{13}C urea in the glassy matrix at 80 K. We demonstrated the operation of the system with acquisition of multidimensional spectra of cross-linked lysozyme crystals which are insoluble in glycerol-water mixtures used for DNP and samples of RNA.

1. Introduction

Cryogenic magic-angle-spinning (MAS) dynamic nuclear polarization (DNP) [1–4] have stimulated a great deal of interest due to the significant sensitivity gain achievable in comparison to the standard room temperature NMR. Polarization enhancements (^{1}H$\varepsilon_{on/off}$) of up to a factor of 658 are possible for ^{1}H, and more for most other nuclei, by employing suitable mono- and biradical polarizing agents [5–10]. When integrated with dipole recoupling experiments [11–20] they have produced structural data that is either difficult to obtain or otherwise unavailable. Because of this success DNP/dipole recoupling experiments are being pursued in many labs around the world [21–24]. However, these experiments generally require special instrumentation – probes, gyrotrons, specially designed corrugated wave guides, cryogenic systems, etc. – which are under active development [1–5,25–43]. In this paper we describe our most recent contribution to this art with the design and construction of a DNP-MAS probe with a special focus on the development of a modular, triple resonance, transmission line system that is balanced on all three channels. In addition, we describe its integration into a 500 MHz/330 GHz DNP/NMR spectrometer utilizing a frequency tunable gyrotron.

The radio frequency (RF) circuitry used in NMR probes may be classified into two categories based on whether the tuning/matching network is in close proximity to the sample coil (*local tuning*) or is at the end of longer RF transmission lines (TL) (*remote tuning*) as pioneered by Schaefer and McKay and Cross et al. [44,45]. Locally tuned probes are typically more compact and lighter compared to remotely tuned probes, which explains much of their commercial appeal. However, locally tuned probes, particularly for narrow bore magnets, typically employ circuits that utilize a variety of small chip capacitors which inevitably fail, leading to catastrophic arcing when high RF power is applied. TL probes typically

---

* Corresponding author.
E-mail address: rgg@mit.edu (R.G. Griffin).

https://doi.org/10.1016/j.jmr.2019.106573
1090-7807/

circumvent this problem by removing the tuning and matching circuits from the bore where more robust components with higher working voltages can be utilized. Concurrently, this strategy addresses the requirements for temperature handling capabilities. In particular, during low temperature MAS-DNP experiments, the sample chamber is cooled to cryogenic temperatures, and common electronic components are either not designed to operate at such temperatures or their electrical characteristics may change substantially, thus affecting the tuning, isolation and coil balancing (*vide infra*). In case of the remotely tuned configuration, most of the temperature sensitive elements can be removed from the cryogenic area, making the circuit more robust and stable. Finally, TL's can be used as electrical impedance transformers which are more efficient than lumped elements at transforming impedances at high RF frequencies. For these reasons, transmission line probes offer clear advantages for MAS and cryogenic DNP experiments [44–50].

Another essential feature of high frequency (≥500 MHz) probes is that the circuit be balanced with an impedance node at the middle of the RF coil, preferably at all of the operating frequencies. At a given frequency, balancing provides improved RF homogeneity and hence more efficient polarization transfer with improved sensitivity [48–52], a characteristic that becomes increasingly important at RF frequencies above 500 MHz. Balancing also reduces the voltage with respect to ground for any given RF field, and this allows for higher excitation powers and Rabi fields before arcing occurs to surrounding grounded conductors, for example, a metallic waveguide that delivers microwave irradiation to the sample during DNP experiments. In general, it is a challenge to design a multi-channel transmission line probe balanced on all the channels due to the fact that it is difficult to measure impedances or scattering parameters directly at the impedance nodes or any other desired position within the probe. Hence most of the previous designs employed lossy LC traps to achieve better isolation between the channels.

The unique approach employed in constructing the probe described here is that it involves attachment of coaxial ports on each module of the probe. Thus, it is possible to measure the scattering parameters of the sample chamber, the TL's, and the tuning and matching modules individually and to adjust them to efficiently interface with the other components. This approach circumvents much of the iterative empirical adjustments ordinarily associated with probe design and construction. It also enables the modules to be interchanged, for example, if a different frequency or rotor size is required. Finally, in order to tune and match the probe and balance the sample coil at multiple (in this case three) frequencies, it is necessary to attach the tuning/matching and balancing networks each to an impedance node on a TL that connects these networks to the sample chamber. This is accomplished by using the transmission line as an impedance transformer where the common node at the three (or more) frequencies is obtained by carefully designed steps of the outer diameter of the inner conductor. The modular design includes an easily detachable and swappable sample chamber/stator assembly, and swappable tuning and matching circuits for different frequencies without modifications to the remainder of the probe etc.

2. Balanced triple resonance transmission line probe for DNP

2.1. RF circuit design

Fig. 1 shows a simplified schematic diagram of a triple resonance balanced RF circuit where the "top probe", consisting of the sample chamber and two transmission lines, is symmetric with respect to the RF coil, except for the inconsequential asymmetry due to the magic angle orientation of the coil itself. The left TL connects to the tuning/matching circuit while the right TL is for the balancing components. The three different branches on each side correspond to the three different working frequencies of the probe. These parallel branches are joined together at the 4-way tees that connect to the main transmission line. Each branch of the RF circuit is tuned and balanced for a narrow frequency range. An RF signal at a particular frequency arriving at the junction point, denoted with a large dot (●), experiences a minimal impedance on the tuned branch and a much higher impedance on other branches. Hence, the signal flows mainly through the tuned branch. The junction points act as common impedance nodes, and provide mutual isolation between the channels, and allow independent design and characterization of the modules and branches. Furthermore, the symmetry of the circuit simplifies creation of a common impedance node at the middle of the RF coil which is necessary to balance the coil simultaneously on all three channels.

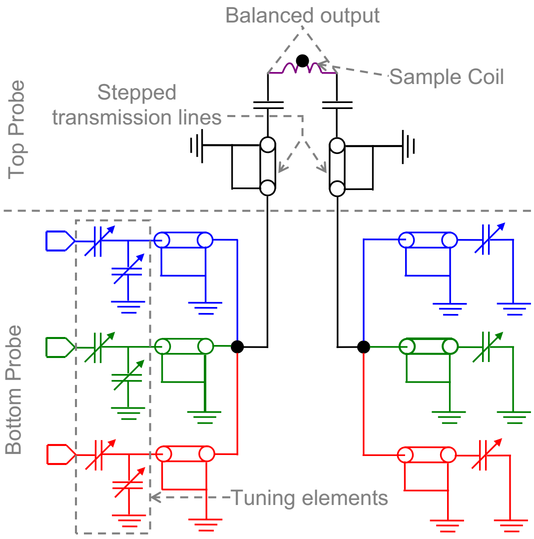

Fig. 1. Simplified schematic of a balanced triple resonance RF circuit. Different colors indicate three different working frequencies. The RF circuit of the top probe is symmetric with respect to the solenoid sample coil. The system is divided in a tuning /matching side (left) and a balancing side (right). Black dots (●) corresponds to common impedance nodes.

2.2. Probe modules and accessories

Fig. 2 consists of photographs of the various components of the balanced $^{1}H/^{13}C/^{15}N$ triple resonance transmission line probe that was built for MAS DNP applications at cryogenic temperatures. This probe has a symmetric modular design consisting of two major components, which we refer to as a "top probe" and "bottom probe". The bottom probe contains tuning/matching and balancing RF circuit elements for three different frequency channels. The transmission lines from the tuning/matching and balancing modules for each frequency are connected to four-way tees connecting the three tuning/matching or balancing modules. The fourth remaining port of the tees connect to the transmission lines of the top probe. From there the main transmission lines in the top probe proceed inside the body of the top probe and connect to the sample chamber. Each individual RF module of the probe is equipped with TL ports following our custom designed coaxial standard connector (*vide infra*).

In operation, the top probe inserts into the magnet and is equipped with a swappable sample chamber at the top which currently uses a 3.2 mm MAS stator, with a removable cap that is used as the constant low temperature oven of the chamber. Vacuum jacketed transfer lines for bearing, drive, variable temperature

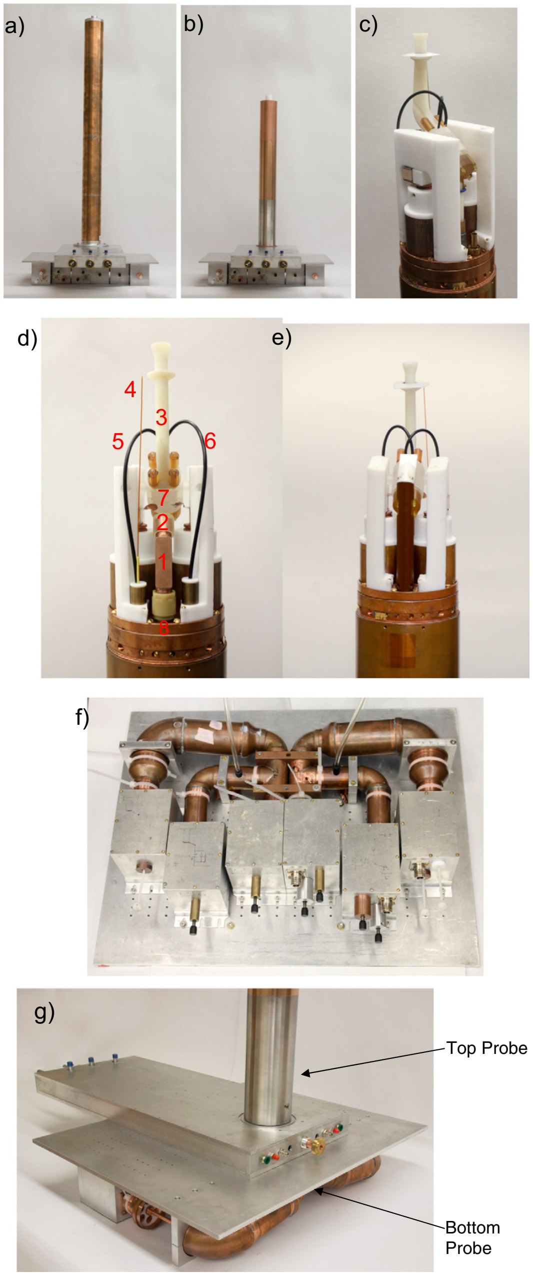

Fig. 2. Various parts of the probe (a) Probe with cryostat; (b) Probe without cryostat; (c), (d) and (e) Sample chamber upon removal of the sample chamber cap, three different views; (c) VT line is not connected in this photograph (d) 1. Wave guide, 2. Lens, 3. Eject pipe, 4. Temperature sensor, 5&6 spin detection fibres, 7. Stator housing, 8. Sample chamber base plate / compression plate; f) Tuning/matching and balancing circuits in the bottom probe; (g) Back of the probe with connectors for purge gas (green), spinning (red), temperature sensing (silver) and microwaves (brass). The evacuation ports of the cryogen transfer lines are visible on the left (blue), and extend beyond the NMR magnet and are accessible during operation. Some of the transmission lines are left open in this photograph. (For interpretation of the references to colour in this figure legend, the reader is referred to the web version of this article.)

(VT) and purge gases as well as the spinning detection cables, temperature sensors, an evacuation line, and the corrugated wave guide for microwave delivery are connected to external devices at connectors at the top probe. Only the main RF transmission lines and the magic angle adjustment rod are interfaced with the bottom probe. This modular design allows the top probe to work with the same bottom probe but utilizing a different stator, or the same top probe can function with a new bottom probe operating at different RF frequencies. In either case the modular inner conductors of the top probe may need adjustment or replacement if they are not already designed for the new system frequencies or stator. Thus, these features were incorporated in the design to address one of the shortcomings of previous transmission line probes which are essentially fixed frequency.

A custom-built cryostat permits efficient cooling of the sample and routine operation down to 80 K. Furthermore, the sample eject and exhaust tubes are vacuum jacketed to reduce thermal losses during operation and sample exchange at cryogenic temperature. Further details about the mechanical design and various probe modules are given in the supplementary material.

3. Novel transmission line – type N adaptors (TL-N Connector) for the characterization of the probe

3.1. Design of transmission line – type N connector

The general challenge in developing a fully balanced multichannel TL probe is to provide a minimally perturbing mechanism to connect to the components of the probe circuit so that the impedances and S-parameters of that component can be measured experimentally. Our modular probe design addresses this problem with individual sections equipped with custom designed TL ports that provide such access points. To connect to these ports, we have designed a set of four TL adapters which mate with TL ports on one end and standard Type N-connectors on the other end. The design and characterization of these TL adapters is discussed in detail in this section.

A set of four identical transmission line connectors each with a Type-N connector (TL-N adapters) were fabricated based on our custom design that allowed accurate measurement of impedances and scattering parameters at any port in the probe. A photograph of the adapters and a schematic drawing is shown in Fig. 3. One end of the TL-N adapter has a standard type-N connector while the other end has a custom designed 50 Ω co-axial transmission line connector so that it mates with the TL ports in the probe. While both ports have a characteristic impedance of 50 Ω, the major and minor diameters of the TL and the type-N connector are very different. Any discontinuity in a coaxial transmission structure will in general introduce reflections. The better the adapter design, the lower the reflection coefficient will be over the designed frequency range. For the case considered here, it was important that the adapters behave like perfect 50 Ω coaxial cables from 10 MHz to 600 MHz and in particular at the design frequencies of 50, 125, and 500 MHz. This allowed us to use the method of port extensions to eliminate the adapter characteristics from S-parameter measurements by numerically extending the location of the port. This is done by moving the reference plane of the VNA to the device under test by applying the electrical delay of each adapter to the measurement and thus removing the phase shift caused by the adapter. Further details on this process are included in Section 11 of the SI. We also constructed custom VNA calibration standards for the TL adapters to remove their characteristics from the measurements with higher accuracy.

Geometrical optimization of the TL-N Adapters was performed using the High Frequency Structure Simulator (HFSS) simulation program. For that a realistic, parametric adapter model was created that very closely resembled the geometry of the type-N connector up to its reference plane as discussed in the next section. The HFSS model corresponded to two adapters connected to each other at the TL ports as shown in Fig. 4 and was designed with the goal of minimizing the reflection of the assembly at the target frequencies of 50, 125, and 500 MHz. The major inner diameter (ID2 = 1.291″) of the TL section was defined by the 1.375″ OD

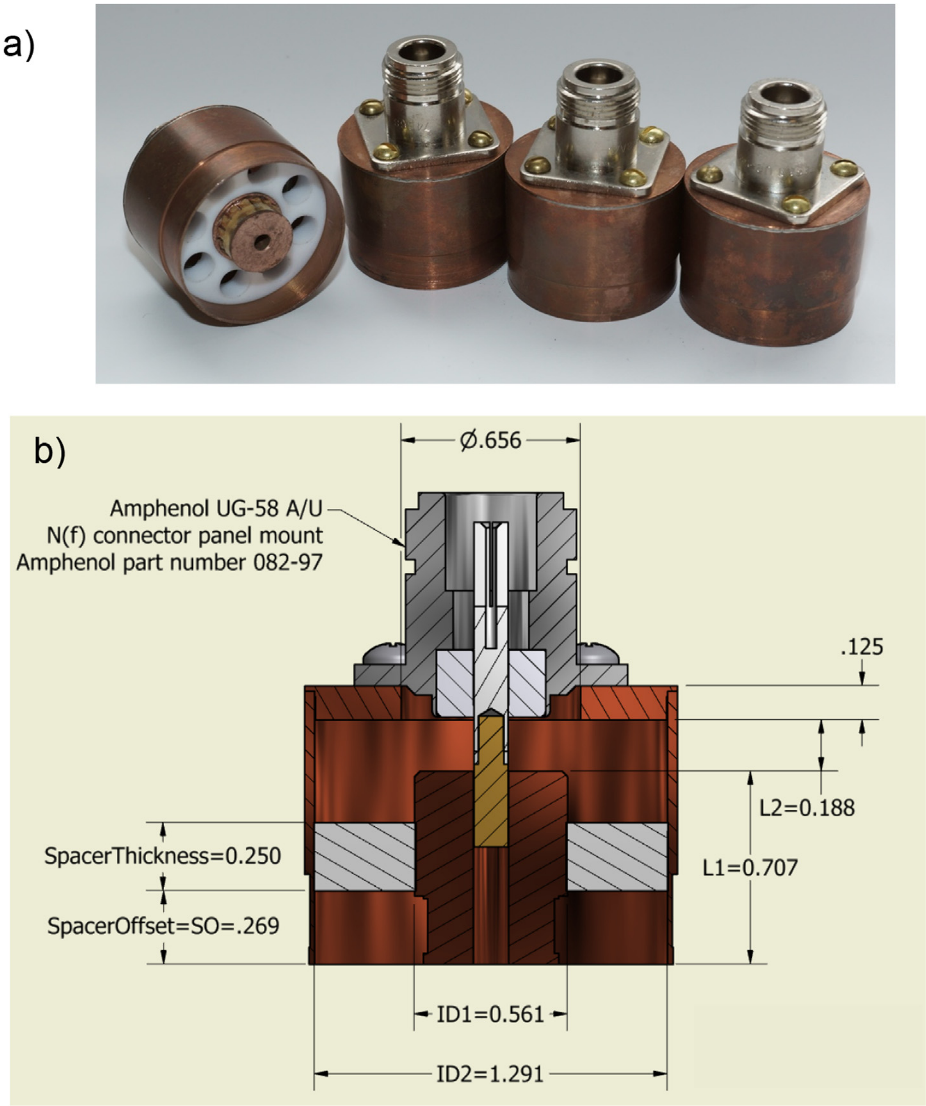

Fig. 3. Adapters from the custom designed 50 Ω transmission line standard 50 Ω type-N connectors (a) photograph of TL Adapters (b) Schematic of a TL adapter (all dimensions in inches). These adapters were used to measure impedances and scattering parameters of probe modules.

copper tubing used in the transmission line of the top probe. Since the adapters are required to have 50 Ohm impedance in the TL port, this defines the diameter in the internal sleeve (ID1 = 0.561″) which extends for 0.25 in. into either mating adapter.

To minimize the reflections over the 10–600 MHz bandwidth of the connector three parameters were iteratively varied with grid searches; specifically, (see Fig. 4) (1) the length of the TL inner conductor L1, (2) the position and thickness of the PTFE spacer disk and (3) the length L2 which defines the length difference between the outer and the inner TL conductor. In the final design stage we fixed L1 to 0.707″ and the spacer thickness to 0.25″. Subsequently, the position of the spacer disk and the length L2 were varied for a final grid search followed by a conjugate gradient minimization of the reflection at 500 MHz (−48 dB). This solution also had optimal or close to optimal reflection at 50 MHz (−62 dB) and 125 MHz (−54 dB), the ^{15}N and ^{13}C frequencies. Over the whole range from 10 to 600 MHz reflection of the designed adapter pair is better than −47 dB. The insertion loss of the connectors, defined as 10logs (P_{trans}/P_{inc}) at 500, 125 and 50 MHz is −0.0014, −0.0022, and −0.0052 dB, respectively.

3.2. Characterization of transmission line – type-N adapters

The purpose of the connectors is to permit measurement of the impedance of a load at a desired reference plane. An approach to performing this measurement is to assume that the adapters are lossless and have a perfect 50 Ω characteristic impedance. It is then possible to apply the method of port extension to measurements using a calibrated VNA with type-N connectors. However, in order to do this measurement properly, the electrical delay of the adapters must be measured and incorporated into the analysis.

To measure the electrical delay of the adapters they were labelled as A1, A2, A3, and A4. The dual-port, single-source VNA (Hewlett Packard 8712ET) was equipped with high quality type-N cables on both ports. The cable on the transmission port had a 20 dB, type-N attenuator (Narda 757C) connected at its measurement side of the cable. After calibration of the VNA, this attenuator's type-N(m) connector and the type-N(m) connector of the cable and the reflection port provided the reference planes. The electrical delays of all possible adapter-adapter combinations were measured using the phase-offset feature of the VNA. These delays

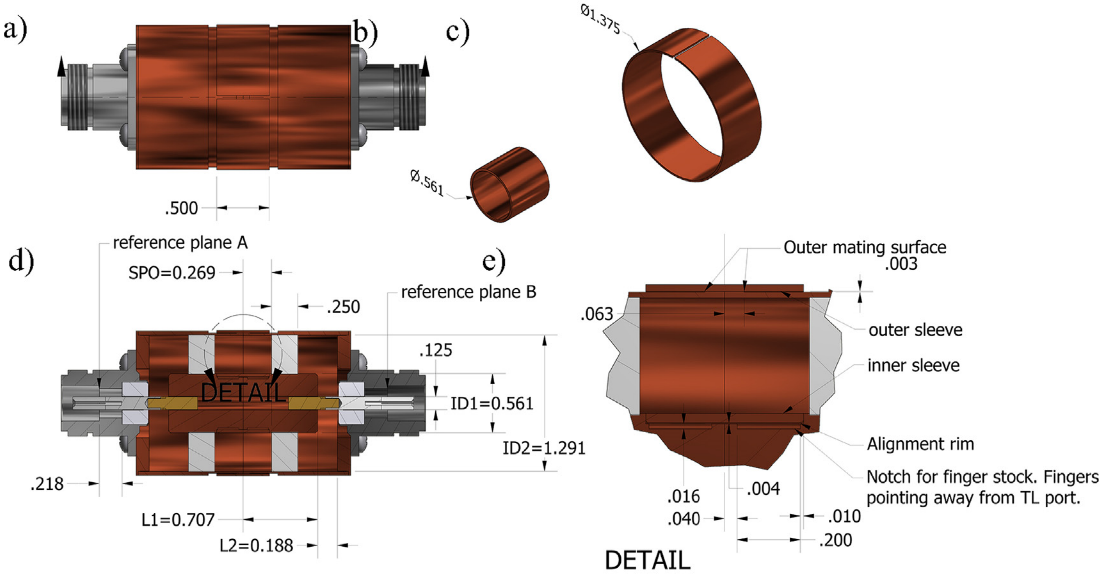

Fig. 4. Adapter design resulting from geometry optimization in HFSS. Shown are (a) two adapters connected to each other at the TL ports, corresponding to the models used during optimization in HFSS, (b) the internal and (c) external connecting sleeve. In (d) the dimensions of the optimization result and in (e) details of the connector interface are given.

report on the combined lengths of two adapters. To derive a good estimate for the length of each single adapter a system of linear equations and the Moore-Penrose matrix pseudoinverse was used (see Supplementary Material, Section 10). The calculated electrical delays at 500 MHz for adapters A1 to A4 are 158 ± 0.4 ps. The standard-error is estimated to be below 5 ps (~3%). The return loss for all adapter pairs is better than 31 dB at 500 MHz, 40 dB at 125 MHz, and 43 dB at 50 MHz. In comparison, the return loss of a Keysight Nf-Nf calibration kit adapter is 43.3, 43.4, and 44.0 dB for 500, 125 and 50 MHz, respectively. The scattering parameters of all adapter pairs are virtually the same, which means that the fabricated adapters are essentially identical, and therefore interchangeable. Thus, they perform well in determining scattering parameters of low-loss devices up to 500 MHz.

Nevertheless, the performance at 500 MHz could be improved and the electrical delay, while flat at the design frequencies, has a +15/−40 ps ripple upwards of 200 MHz, which could complicate data analysis and system modelling. For this reason, we decided to define new transmission line calibration standards so that the calibrated *reference plane of the VNA would be directly at the open TL end of TL-adapters, which are connected to the type-N measurement cables*. We chose adapter A3 in combination with calibration standards (open, short, load) of the Keysight Type-N calibration kit (85032F) to define new calibration standard. The zero-length through standard was provided by simply connecting the sexless adapters to each other.

First, the pair-wise S-parameters of all possible 6 adapter-adapter combinations were measured. Due to the reciprocity of the adapters, and the small but measurable differences of the adapters, this provided 18 known, independent parameters for each of the linearly spaced 1601 frequency points between 10 and 600 MHz. The total number of unknown parameters for the 4 different adapters is 12. Thus, the experiments provided sufficient data to determine the S-parameters of the individual adapters. For accurate results we used the process of de-embedding which allows us to extract the performance of the adapter by eliminating the effects of the internal features of the network analyzer and the other components used during testing. (See Supplementary Material, Section 8) For de-embedding we used Advanced Design System (ADS) from Keysight and its optimization features. The S-parameters of in-silico adapters, connected to each other in all 6 possible pairs, were optimized so that the difference of the S-parameters of the matching experimental and in-silico adapter pairs was minimized. This yielded the S-parameters of all individual adapters for all frequencies. In the process small deviations from reciprocity and passivity of the adapter pair measurements were corrected where appropriate.

Next, the scattering parameters of one adapter pair and several calibration standards, A2-A3-cal, were measured for all of the short, open, and load N(m) standards from the Keysight kit. In each case the properties of adapter A2 were removed by a t-parameter de-embedding approach, using the known S-parameters of A2, and a custom code in MATLAB. This yielded the S-parameters of the new calibration standards A3-cal for all frequencies. Again, small deviations from reciprocity and passivity of the adapter pair measurements were corrected where appropriate. In some VNA's these scattering parameters can be directly used as calibration standards. Here, we used the S-parameters to parameterize our new TL standards using parameters according to the published calibration standard model of our VNA (Agilent 8712ET). For fitting, only the frequency ranges 49–51 MHz, 124.5–125 MHz, and 475–525 MHz were used to emphasize accuracy at the ^{15}N, ^{13}C, and ^{1}H frequencies. Keysight does not publish an explicit mathematical model for the load but only gives the parameter names: characteristic impedance, delay, and loss. The load model represented a lossy TL with a 50 Ω termination and we used a corresponding mathematical description for fits to find initial parameters. The parameters of the load had to be iteratively fine-tuned using the VNA itself. Fitting the published "open" model to the experimental S-parameters yielded a very good fit with deviations smaller than 2.5×10^{-3} in the target frequency ranges. The published short model deviated by less than 4×10^{-3} and the load model by less than 2×10^{-3}. After calibration, using the TL adapters and their characteristic parameters, the reflection TL port should measure exactly the same S-parameters for each adapter as the ones resulting from de-embedding. The load parameters were optimized manually so that after calibration with all parametrized standards the measured S-parameters at 500 MHz matched the de-embedded counterpart. Numerical fitting for characterization of the new calibration standards was done in MATLAB using multidimensional unconstrained nonlinear minimization (Nelder-Mead).

Our new TL calibration standards were used to measure the scattering parameters of one of the 4-way tees. The same parameters were also measured using only port extension and were simulated using HFSS. A comparison of the different results allowed an assessment of the accuracy of the measurements. For the measurements, the 4-way tee was mounted in the same fixture that was later used in the bottom probe including the clamps which firmly and reproducibly connect the adapters to the tee. The experimental assembly is shown in Fig. 5. Using our two-port, single-source VNA made it necessary to terminate the unused ports of the tee with 50 Ω loads. For that we used TL adapters with 10 dB and 20 dB Narda precision attenuators in conjunction with precision 50 Ω loads. Their combined load match was better than −43, −47, and −50 dB for the ^{1}H, ^{13}C and ^{15}N frequencies, respectively. The slight reflectivity of these aggregate TL loads will have biased the measurements to a small degree and was not removed. Both, the measurement with port extension and the one using TL calibration standards, reproduced the simulated S-parameters well (Fig. 5b). But still, in particular for reflection, the measurements were improved considerably using the VNA calibration with our new TL standards. Considering the small deviations of simulation and experiment, using the TL calibration standards, it is hard to say if the deviations between the measurements and simulation originate in simulation inaccuracies, measurement errors, or deviations of the simulated and fabricated geometry.

3.3. Measurement of the electrical arm length of the four-way tee

The center of the four-way tee acts as the common impedance node for the three channels on either side of the probe. While the impedances at the branching point in the center of the 4-way tee cannot be measured, it is still possible to approximate their values by measuring impedances on one of the ports of the tee and applying an appropriate port extension, matching the electrical delay, or “arm length”, from the port to the center. The delays of the arms are also needed to design the main transmission lines and pre-adjust the balancing and tuning modules. Our approach assumes that the sections of the tee from any port to the center will behave like a 50 Ω transmission line. In general, these electrical delays are frequency dependent. To determine the effective electrical delays from each of the ports to the center of the tee we used a similar approach to that used for determining the electrical delays of the TL adapters. In particular, the electrical delays from each port to all the others was derived from the experimental S-parameters, a system of linear equations was solved, and the Penrose-Moore pseudo inverse was used to determine the length of all the arms of the tee (see supplementary material). We assumed that the effective electrical delay of each arm is independent of which other arm is chosen for delay measurement. This assumption is not strictly correct, as the electrical delays calculated from sums of delays of individual arms deviate by up to 18.5 ps from the experimental values (sums) corresponding to a length of 5.4 mm. To simplify measurements these individual-arm lengths (the arm length is defined as the distance from the center (branching point) to any one of the four faces) were used without modification. As

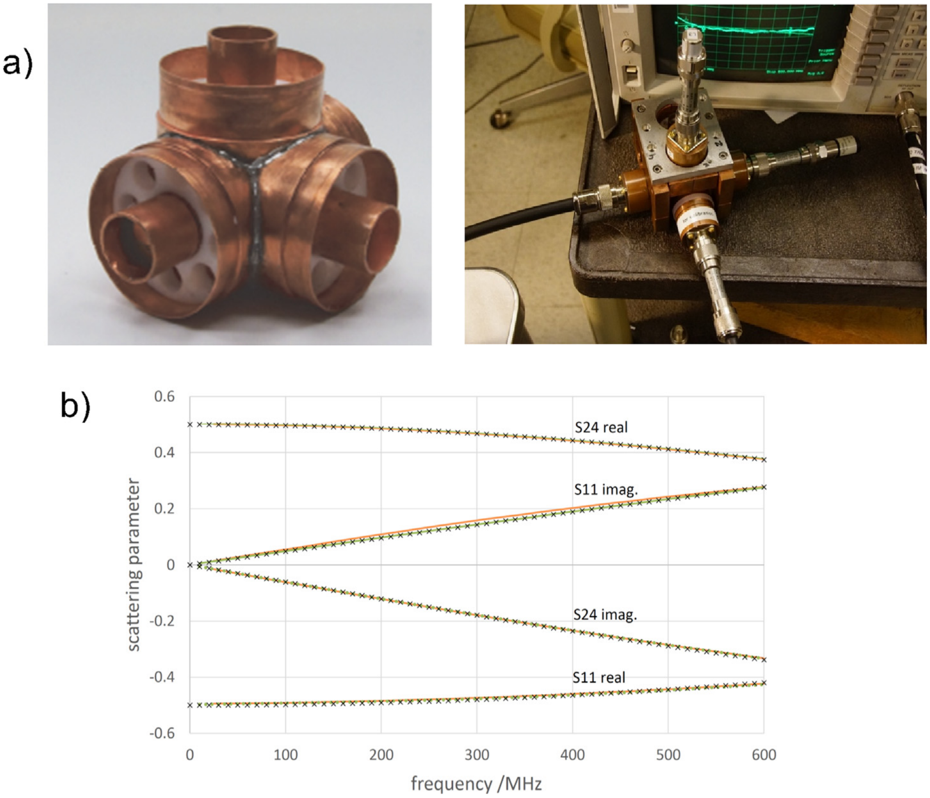

Fig. 5. (a) (left) 4-way tee showing the construction of the ports to which the three RF channels and the transmission line are connected. Additional details on the design and construction of the tee are available in the Supplementary Information, Section 12 and Figure S32. (right) Experimental assembly employed to measure scattering parameters of the 4-way tee from port 4 to port 3. (b) Comparison of simulated (x) and measured scattering parameters using port extension (orange) and the parametrized TL calibration standards (green). (For interpretation of the references to colour in this figure legend, the reader is referred to the web version of this article.)

the center of the 4-way tee has a dimension larger than 5.4 mm these lengths should still provide good estimates for port extensions. The derived delays for individual arms vary only by no more than 0.95 ps between frequencies. We used the single-arm delays at the proton frequency for all measurements as this is the channel requiring the highest accuracy in adjusting impedances. Port 1 is defined as the connection to the main transmission line of the top probe. If the tee is viewed from above, with port 1 pointing upwards and the other ports are aligned like the letter T and they are numbered in a clockwise fashion, starting with the right port (port 2). The calculated delays for port 1 through port 4 are 76.21, 86.92, 76.24, and 86.88 ps.

4. Design and construction of the probe

In the construction and characterization of the probe we have employed an iterative stepwise process consisting of four basic steps focused on

(1) the sample chamber stator and NMR coil,
(2) the transmission lines connecting the sample chamber to the four-way T,
(3) the bottom probe dimensions and
(4) integration of the three major components.

We now discuss each of these in detail.

4.1. Characterization of the sample chamber

Generating a current maximum (or a voltage minimum) in the center of the sample coil at a certain frequency is generally referred to as “balancing” the channel. To facilitate balancing, the top probe was constructed to be essentially mirror symmetric with respect to its mid plane. This is particularly important for the sample chamber, containing the MAS rotor, the RF coil, the stator, MAS adjustment devices, capacitors, stator posts, etc. However, the complexity of the sample chamber limits the accuracy of any simulation of S-parameters or internal electric and magnetic fields, to derive the impedances which are to be applied to the input and output ports to achieve balancing. (Here we define the input port as the port belonging to the balancing side of the probe). Thus, it is not possible to *a priori* determine the input impedances for the three frequencies which have to be applied to the sample chamber to maximize the current through the coil. If the sample chamber is symmetric, and if the center of the coil contains a current maximum (and in turn an impedance minimum at almost ground potential) then the balancing input and output impedances will be approximate complex conjugates of each other. We used this fact to determine the balancing input and output impedances of the sample chamber from measured S-parameters.

4.1.1. Scattering parameters of the sample chamber:

To measure the S-parameters of the sample chamber, we initially used smooth wall inner conductors for the main transmission lines (connected directly to the sample chamber) with a diameter chosen to adjust the characteristic impedance of the assembly to 50 Ω. This allowed us to use **simple port extensions** to remove any offset effect of these TLs on the measurements. We then also measured all the two port S-parameters for both of the lines so that any effect on measurements could be removed via de-embedding procedures more accurately. These main transmission lines partially become part of the sample chamber as they extend into it. On their capped top they encounter stray field effects and no longer behave like ideal 50 Ω lines, effects that were included into the sample chamber S-parameters. For this purpose, the reference plane of the sample chamber ports was not defined by the end of the line, but instead was placed 0.5″ (12.7 mm) below the upper end of the transmission lines. The effect of these 0.5″ extensions was removed from the measured scattering parameters of the 50 Ω transmission lines by applying a simple port extension during their characterization. Following complete assembly of the top probe and using a glycerol filled sample container, we again measured the scattering parameters on the two ports which are connected to the bottom probe. Then the scattering parameters of the two 50 Ω transmission lines up to the reference planes were removed via **de-embedding**. The resulting scattering parameters of the sample chamber were very symmetric. A set of four measurements were performed using 10, 20, 30, and 40 pF capacitor (arrays) in series with the coil on both sides. As the 40 pF capacitors produced a resonance close to the ^{13}C frequency we chose them for the final probe.

The length of the main transmission lines should be estimated beforehand to allow propagation of the impedances to the common null points at the centers of the 4-way tees. If the capacitance is too small, yielding a high reactance, then the length of the line can approach a quarter wavelength. Because of the difficulties of modelling the sample chamber *a priori* this task is difficult. Thus, to be on the safe side the design of the main transmission lines and the cryostat should be finalized only after characterization of the sample chamber, using provisional 50 Ω transmission lines.

4.1.2. Determination of the balancing condition

Using the experimentally measured scattering parameters of the sample chamber, we determined its balancing impedances for which the complex conjugate of the output impedance is equal or close to the input impedance. For this purpose, the 2-port scattering parameters were used in an APLAC circuit simulation model where we chose a range of purely reactive input impedances and determined the resulting output impedances for each operating frequency. The input impedances for which the magnitude of the difference to the complex conjugate of the resulting output impedance was minimized were used as estimates for balancing impedances. This procedure was repeated using MATLAB and the “Electromagnetic Waves and Antennas” toolbox [53] with a higher precision. The resistive component of the input impedance is ignored here, as it will be small. For every probe frequency two balancing impedances were found. One maximizes the current in the center of the coil and also maximizes the voltage difference over the coil, which is the desired solution. It also minimizes the voltages with respect to ground in the vicinity of the coil. The other solution is undesirable and minimizes the current in the center of the coil and minimizes the voltage difference over the coil. Results illustrating the balancing are tabulated in column three of Table 1.

4.1.3. Maximizing the current at the center of the RF coil (balancing of the RF coil)

While it may be possible to rationalize which of the two solutions obtained from the balancing-simulations will maximize the current for each frequency, assuming a certain behavior of components inside the sample chamber, we chose to experimentally verify the character of the solution. Thus, we chose an approach that allowed us to measure relative voltages and phases on the left and the right lead of the coil. Voltage measurements were performed on a modified top probe which had the sample chamber cap removed and replaced by a sheet of copper foil (provisional cap) of equal size. The provisional cap, which emulated the electrical behavior of the actual cap to a high degree, had a window which allowed a voltage probe to reach the coil leads on either side just outside the stator. For these measurements, the top probe was equipped with the aforementioned 50 Ω main transmission lines.

Table 1
Results of voltage measurement that identify balancing conditions.

Nucleus	Freq./MHz	Calculated Z_{in} Ω	Measured		V_{left} mV	V_{right} mV	Phase deviation	Maximum condition
			Z_{in}/Ω	Z_{out}/Ω				
^{1}H	500.058	116.699 j	117j	7.5 − 116j	−14.4	8.6	7.2°	current
^{1}H	500.058	53.2999 j	+53j	3 − 57j	−17.0	−17.4	7.2°	voltage
^{13}C	125.739	−12.0804 j	−12.04j	2.5 + 13.2j	0.30	−0.30	−9.8°	current
^{13}C	125.739	280.187 j	+280j	37–361.9j	58.8	44.4	0°	voltage
^{15}N	50.670	57.3798 j	0.85 + 57.0j	2.6–58.5j	+344	−356	−2.412°	current
^{15}N	50.670	717.556 j	230 + 717j	155 − 565j	25.2	24	0°	voltage

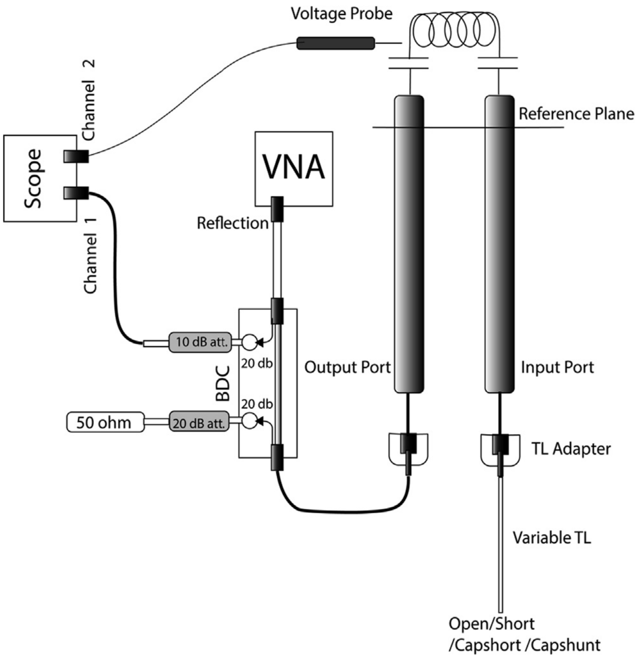

Fig. 6. Schematic diagram of the instrumentation for characterizing the balancing conditions of the RF coil.

The instrumentation for characterizing the balancing condition is illustrated in Fig. 6. The output port of the top probe was connected to a TL adapter (providing the calibrated reference plane for CW VNA reflection measurements), a type N cable, and a nominal 30 dB bi-directional coupler which was connected to the reflection port of a VNA. About 20–30 dB of the 16 dBm power output of the VNA was redirected by the directional coupler, attenuated by another 10 dB, and then fed to one channel of a digital oscilloscope (Tektronix TDS 3052). This signal provided a phase reference and was used for triggering voltage measurements. The other port of the bidirectional coupler was terminated with a precision 20 dB attenuator and a 50 Ω load. The high attenuation and good termination on the ports of the bidirectional coupler make the VNA measurements independent of any oscilloscope settings or external influences. The input port of the top probe was connected to a variable transmission line (General Radio Co. Type 874) via a TL adapter. The variable transmission line was adjusted to create the desired input impedances in the input reference plane of the sample chamber. For this the transmission lines were, on their terminal side, either shortened, left open, or equipped with a series capacitor or shunt capacitor.

First, to adjust the length of the variable transmission line so that the correct input impedance was created in the input reference plane of the sample chamber, the TL adapter on the VNA side was connected to the TL adapter on the variable TL line. A port extension of −1.819 ns was applied which corresponds to the electrical length of the 50 Ω TL minus 0.5 in. Thus, effectively, the VNA measured the input impedance to the sample chamber as provided by the variable TL assembly and the 50 Ω TL inside the top probe. This impedance was adjusted to correspond to one of the calculated, required input impedances at their respective frequencies. Following this, the adjusted variable TL was connected to the input port of the probe and the TL adapter on the VNA side was connected to the output port of the probe. The port extension was adjusted to + 1.819 ns. Now the VNA measured the output impedance of the sample chamber in its output reference plane. If the correct input is provided the output impedance should be almost equal to the complex conjugate of the input impedance.

Using this instrumentation the impedance of the sample chamber was measured first without using the voltage probes and having Z_{in} adjusted to +57.76j Ω at 500.05 MHz, with the original sample chamber cap (Z_{out} = (2.545–58.14j) Ω), without sample chamber cap (Z_{out} = (10.59–109.7j) Ω), and with the provisional sample chamber cap (Z_{out} = (2.54–59.76j) Ω). Thus, the importance of using a provisional cap is clear and that the provisional cap introduces virtually no measurement error.

Similarly, the performance of the voltage probe was evaluated. The voltage measurements provided sinusoidal signals from the reference channel and from the voltage probe. This allowed measurement of the voltage difference and phase shift of voltages on the left and right leads of the sample coil. During the voltage measurements the voltage probe and the RF probe become one electric system. Thus, the voltage probe has the potential to alter the measurement result. For some measurements the 350 MHz probe was used unaltered. In particular, for measurement at 125 MHz or 500 MHz a tip resistor with a resistance from 1 MΩ to 20 MΩ was added. The sensitivity of the circuit to change upon connecting the voltage probe depends on the impedance of the NMR probe at the location of contact. If the impedance is low, e.g. for current balancing conditions, the circuit is insensitive, and if the impedance is high it is sensitive to voltage probe contacts. The admittance of the voltage probe to ground has to be much lower than the admittance of the NMR probe at the point of measurement. The influence of the voltage probe on the NMR probe can always be monitored on the VNA, as it continuously measures the impedance on the output port of the probe. If this impedance changes too much upon voltage probe contact, a larger tip resistor has to be used. In all these measurements it is important to have a low resistive part of the input impedances. Otherwise voltages and phases become less symmetric. Also it is important to only have a single harmonic in the signal from the VNA. Otherwise not only the voltage of the balanced, wanted frequency components will be measured, but the signal will be distorted by contributions at other frequencies which are not balanced in any way. Thus the power of the VNA had to be limited to 16 dBm to suppress harmonics. Results of the impedance and voltage measurements are summarized in Table 1.

4.2. Design of the inner conductor of the main transmission lines

Transmission lines can function as impedance transformers and are used in both the bottom and top probe in this capacity. In particular, the transmission line on the balancing side transforms the minimum impedance at the common impedance node at the 4-way tee to the required input impedance at the input port of the balancing side of the sample chamber. Similarly, the output impedance of the sample chamber is transformed to a minimum at the 4-way tee of the tuning and matching side of the probe. As the input and output impedances of the sample chamber are almost complex conjugates of each other and the direction of propagation is the same in both cases, identical stepped inner conductors can be used in both transmission lines. Stepped transmission lines were designed in MATLAB using the tuning/matching side as a working model. One possible design constraint is that the output impedance to the transmission line can be estimated from the arm length of the 4-way tee and assuming that the impedance in the null point of the tee is zero ohms. The input impedance of the TL for every operating frequency has to match the measured balancing impedances of the sample chamber. Furthermore, the lower section of the inner conductor has to have at least a 0.25 in. section at 50 Ω characteristic impedance to accommodate the transmission line connector. At the top the inner conductor has a 0.5 in. long section at 50 Ω characteristic impedance, which is electrically part of the sample chamber.

Keeping these constraints in mind, a stepped transmission line model of the total required length was created randomly in MATLAB. Pre-determined balancing output impedances of the sample chamber were propagated along the random line which was extended to the impedance minimum in the tuning-matching 4-way tee by applying the electrical delay of arm 1 of the tee (Arm 1 of the four-way tee connects the tee to the sample chamber). For a correctly designed TL the resulting impedances at the resonance frequencies of the three nuclei should all be zero. A score was calculated based on the weighted sum of the magnitude of the impedances at the three frequencies, with the goal to minimize the score. Each model consisted of up to 30 sections of variable length. The characteristic impedance of each section was randomly selected in the range from 10 Ω to 100 Ω, in steps of 3 Ω. For characteristic impedances from 10 to 22 Ω a PTFE dielectric with $\varepsilon = 2.1$ was chosen and for the other sections $\varepsilon = 1$ was used. From the models with the best scores, a few simple ones were chosen by visual inspection for further analysis. For these models we then used HFSS to simulate the electric fields in the line under operating conditions. Models prone to electrical breakdown, as judged by high voltages were excluded. The final model was modified and one section without PTFE dielectric was substituted against one with PTFE but with the same characteristic impedance. Finally, to reduce the risk of electric breakdown at the large (0.877″) diameter section of the inner conductor, we inserted an additional 0.5 in. long PTFE dielectric at each end of this section.

Starting from this manually created model, using fixed dielectric constants for all sections, and observing the length restriction and upper diameter boundaries for the added 0.5 in. PTFE sections, a simulated annealing optimization (SA) of the stepped transmission line was performed to correct for the manually introduced changes to the impedance transform. This was followed by an unconstrained nonlinear optimization, another SA optimization, and another unconstrained nonlinear optimization. The final geometry of the stepped transmission line is depicted in Fig. 7. Finally, the impedance transformation properties were validated in APLAC and HFSS.

4.3. Bottom probe dimensions

As the 4-way tees contain the impedance minima for all frequencies they provide boundary conditions to design, independently of each other, the balancing and tuning/matching modules with their respective transmission lines. The basic bottom probe dimensions were laid out using RF simulations in APLAC. These simulations were based on estimates of the final Q factors for L, reverse L, and PI networks (see supplementary material) as tuning and matching circuits. These provided the required input impedances of the TL ports of the tuning and matching boxes, which in turn determined the lengths and characteristic impedances of the transmission lines from the 4-way tee to the tuning and matching boxes. Similarly, the available space and capacitor sizes defined the length and characteristic impedances of the balancing transmission lines.

4.4. Integration of the bottom probe to the top probe

All the capacitors in the balancing modules were adjusted by using a preliminary assembly of the respective box for a given frequency, mounting the required transmission line, and then measuring the impedance on the end of this TL while applying the port extension to extrapolate it to the center of the 4-way tee. Then the capacitance in the box, using variable capacitors or chip capacitors, was adjusted until this extrapolated impedance was minimized for the desired frequency. The impedance at the other two frequencies was desired to be as high as possible to improve the independence of the balancing modules from each other. If necessary, the transmission line length had to be altered to achieve the latter requirement. Then all the balancing modules were mounted to the bottom probe base plate and connected to the 4-way tee. Again, the impedances were fine-adjusted by measuring the impedance on port 1 of the 4-way tee, extrapolating to the null point. Following this, the top probe, without sample chamber, was connected to the bottom probe with the stepped transmission line

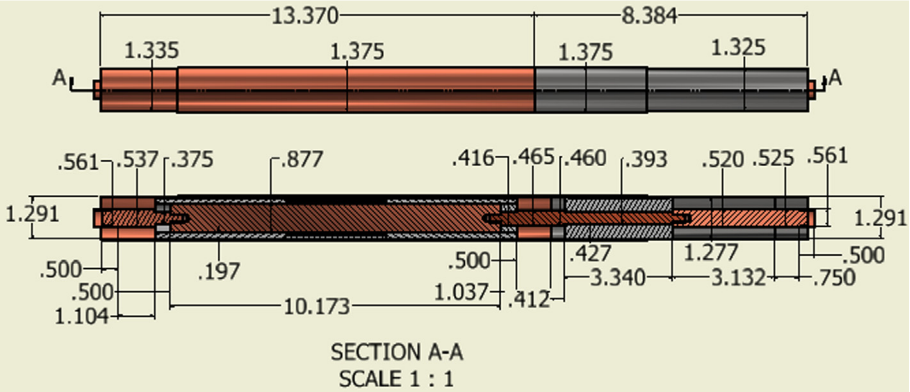

Fig. 7. Top: Main transmission line with the stepped inner conductor protruding from the inside. Gray: 316 stainless steel, Copper: Cu. Bottom: Stepped transmission line, with the left side is on the top. Cross hatched grey: PTFE; Cross hatched copper: Cu. All dimensions are in inches.

Table 2
Measured probe characteristics at room temperature. B_1 field homogeneity was measured without prior shimming.

Channel	Q factor	Rabi freq./kHz	Applied power/kW	Conversion factor/kHz/$\sqrt{W}$	B_1 field homogeneity A_{810}/A_{90} better than:	Tuning range/MHz for fixed balancing capacitance	Isolation/dB
^1H	233	190	2.06	4.19	>0.86	3.41	$^1H \rightarrow {}^{13}C$ – 18.1 $^1H \rightarrow {}^{15}N$ – 17.8
^{13}C	117	280	2.00	6.26	>0.76	5.40	$^{13}C \rightarrow {}^1H$ – 46.6 $^{13}C \rightarrow {}^{15}N$ – 43.7
^{15}N	193	83	2.22	1.77	>0.75	2.4	$^{15}N \rightarrow {}^1H$ – 49.7 $^{15}N \rightarrow {}^{13}C$ – 25.9

on the balancing side and the impedance was measured on the top of that TL using a port extension of +0.5 in.. This measured the input impedance to the sample chamber which was adjusted as closely as possible to correspond to the desired, balancing value. Next the sample chamber was mounted, while leaving the main transmission line on the tuning/matching side at 50 Ω. This allowed verification that the correct output impedances were created and that the sample chamber was balanced.

Next, the transmission line on the tuning side was replaced by the stepped model and the top probe was mounted to the bottom probe, which only contained the balancing modules. The calibrated TL adapters were used to measure the impedance on the bottom of the tuning/matching TL and extrapolated to the center of the TM 4-way tee to confirm that impedance minima would be created there. The impedance on the ^1H channel in the null point was about −3j Ω.

Using a similar procedure to that employed for the balancing modules, the tuning and matching modules were pre-tuned. The electrical delay of each tuning/matching transmission line at its design frequency was measured and the delay of the arm of the 4-way tee to which is was connected was added. Then a variable transmission line with a short on one end (emulating the null point in the center of the 4-way tee on the tuning side) and a TL adapter on the other was adjusted to a length to equal that sum of delays. The adjusted variable TL assembly was connected to the TL port of the tuning and matching module and the tuning elements were adjusted to minimize the reflection that was measured by a VNA connected to the type N port of the TM module. Then the adjusted modules were mounted, together with their transmission lines and the 4-way tee, to the base plate of the bottom probe. Finally, the complete probe assembly was tuned by using the variable capacitors in the tuning and matching modules. Preliminary Q factors and isolations were measured.

To improve the isolation from the ^1H to the ^{13}C channel, due to the slightly incorrect positioning of the proton impedance minimum in the TM 4-way tee, a PTFE slug which slides on the lower section of the stepped inner conductor of the TM TL was fabricated. It was equipped with G10 rods which reach through added drill holes in the bottom of the 4-way tee and permit the adjustment of the position of the slug while measuring isolations and tuning. These rods were removed after adjusting the slug position. The slug is equipped with an internal O-ring to firmly mount it to the inner conductor while allowing manual adjustment of its position. The closer this slug is moved towards the impedance minimum the less it increases the impedance on the ^1H channel. The impedances on the other channels are insensitive to the slug position. The position was adjusted to optimize for $^1H \rightarrow {}^{13}C$ and $^1H \rightarrow {}^{15}N$ isolations.

5. Performance of the probe

The RF performance of the probe is exceptional for the ^{13}C channel, reaching a Rabi frequency of 280 kHz, and is limited by the available power of the used RF amplifier. The ^1H and ^{15}N channels could attain a maximum Rabi frequency of 190 kHz and 83 kHz, respectively, again limited by the amplifiers. No arcing or detuning was observed even for pulses of 1 kW and 200 ms duration. The RF efficiency, isolations and measured Q factors are tabulated in Table 2.

5.1. Ball shift test

The B_1 homogeneity along the RF coil could be measured by the ball shift test. Traditionally this test is performed by monitoring the shift in the tuning frequency by progressively inserting a copper ball along the axis of the coil [48,51]. The shift in the tuning frequency, caused by the conductive perturbation of the metal ball, is directly proportional to the square of the B_1 field at that point. A balanced RF circuit should produce an entirely symmetric shift in the resonance frequency on moving the metal ball to either direction from the center of the coil. Instead of a ball we used a metal disc. To ensure accurate positioning of the disc in the RF coil we have designed a set of PTFE spacer pairs with dimensions to fit into a 3.2 mm RevNMR rotor. Only sample changes and resetting of spacer pairs was required to change disc positions; probe modifications were not necessary. Spacer pairs along with the brass disc (0.584 mm dia / 2.006 mm length) cover the active area of the RF coil (6.35 mm). The resonance frequency as a function of the disc position was measured using a VNA. Results of the ball shift test on all the three channels are shown in Fig. 8. We have a fairly symmetric distribution of the B_1 field on all the three channels. It should be noted that our RF coil for the ball shift test was made of 6.35 mm long silver-plated copper wire (22 AWG) with five turns and a uniform pitch. We could further improve the RF homogeneity by employing a variable pitch RF coil and susceptibility matched wire. Nutation curves are illustrated in Fig. S42.

6. Gyrotron and the corrugated wave guide

In parallel with the development of the HCN probe, a frequency tunable continuous wave 330 GHz gyrotron was developed for DNP application at 500 MHz ^1H resonance frequency. This oscillator operates at the second harmonic of the electron cyclotron frequency with a $TE_{4,3}$ cylindrical mode and offers a tuning range of Δf = 1.2 GHz, maintaining a significant microwave power output. Details concerning the design and operation of the gyrotron are published elsewhere [40]. Operating at magnetic field strength of 5.991 T, with a cathode voltage of 12.5 kV and with a beam current of 160 mA, the gyrotron produces a microwave output power of 12.4 W at 328.942 GHz. For extended periods of operation, the gyrotron is run under PID control to prevent any fluctuations in the output frequency and power. The output Gaussian beam of the gyrotron reflects off the last mirror of the internal mode converter into a periscope assembly. This consists of corrugated waveguides and miter-bends placed outside of the gyrotron.

The NMR magnet and the gyrotron magnet are not shielded and therefore located ~5 m apart to avoid interference of the two fields. A waveguide transmitting the microwave power from the exit of the periscope assembly to the entry point in the NMR probe

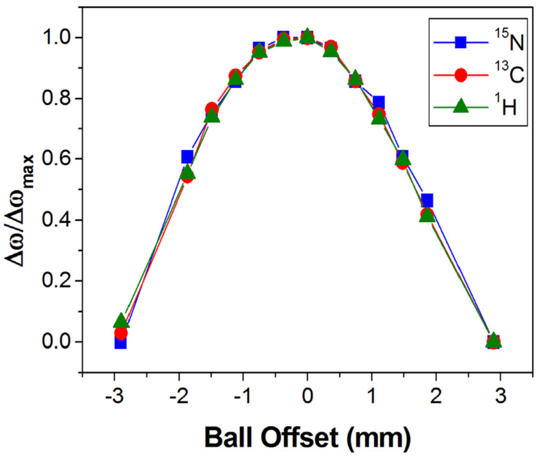

Fig. 8. Ball shift test illustrating the balanced tuning of the coil at all three frequencies – ^{13}C, ^{15}N and ^{1}H.

runs through a distance of 8.3 m with three miter bends inserted at appropriate points. This waveguide is made of brass cylinders of 19 mm i.d. with 30 and 60 cm long sections. Corrugations in the waveguide sections were created by helical tapping using a tap with 80 grooves per inch (3.15/mm) [40]. The last section of the waveguide is down tapered from 19 mm to 8 mm i.d. to match the waveguide inside the probe. Fig. 9 shows the 500 MHz/330 GHz DNP-NMR spectrometer with the gyrotron and the NMR magnets as well as the corrugated waveguide transmission lines between them.

The corrugated waveguide inside the probe has an 8 mm i.d. and has a total length of 50 cm with 9 individual sections made of OFHC copper. The last section of the waveguide radiating the microwave power into the sample chamber is easily removable and has a miter-bend at the magic angle. An optimized bi-polynomic, "ellipsoidal" lens fabricated from TPX [54] is placed at the end of the waveguide to convert the radiating HE_{11} mode of the corrugated waveguide into an elliptical profile beam with almost uniform axial power distribution for efficient coupling to the sample rotor. The lens is depicted in Fig. S43.

Each section of the waveguide assembly was carefully aligned and the insertion losses and microwave beam profile were documented, in hot test, at different positions along the transmission line. We measured ~0.5 dB loss in the ~8.3 m, 19 mm i.d. corrugated waveguides which is in good agreement with our previous cold test measurements of 0.047 dB/m performed using the radiometer technique [55], taking into account the fact that beam quality was better in the cold test setup. The miter-bends encountered ~0.15 dB loss and the 8.5 cm long corrugated downtaper encountered ~0.07 dB loss. The losses in the ~50 cm long, 8 mm i.d. corrugated waveguide, inside the probe, were measured to be 0.65 dB. The overall loss of the entire transmission line from the exit of the gyrotron to the sample rotor in the probe was measured to be 1.4 dB (28%).

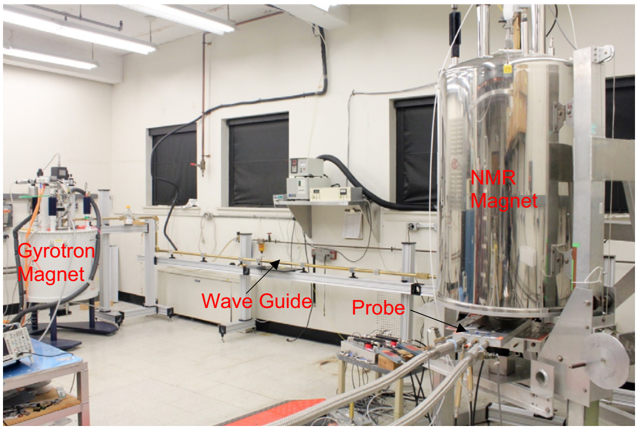

Fig. 9. Photograph showing the configuration of the 330 GHz/500 MHz DNP-NMR spectrometer. The 330 GHz gyrotron is shown on the left in an 8 T Bruker magnet. The 11.8 T NMR magnet is shown on the right.

7. DNP measurements on proteins and nucleic acids

DNP experiments with cross polarization and magic angle spinning were performed on a number of samples with continuous wave microwave irradiation. With the standard DNP sample of 1 M ^{13}C-Urea dissolved in a 60/30/10 (w/w) glycerol-d_8/D_2O/H_2O matrix with 9 mM AMUPol as the polarizing agent, we achieved an enhancement of 180 at 77 K (Fig. 10).

In addition, we recorded DNP enhanced spectra on two different systems that illustrate new applications of DNP to biological systems – cross-linked hen egg-white (HEWL) lysozyme crystals and an RNA, specifically, 2′dG WT-70 RNA [56]. Both systems exhibit well resolved spectra and illustrate the resolution and sensitivity that is possible in low temperature DNP experiments.

Microcrystalline proteins such as ubiquitin and GB1, which are standard samples for development of MAS recoupling experiments [57,58], dissolve in the glycerol/water glassy solution (a.k.a. "DNP juice") that is frequently used as a matrix for DNP experiments and is required to disperse the polarizing agent and cryoprotect protein. Thus, preparation of 'dissolution resistant' samples that maintain their crystallinity [59,60] while being cryoprotected are attractive systems for DNP studies. An approach which could address this problem is cross-linking a protein crystal with glutaraldehyde which is a technique employed in X-ray crystallography to stabilize proteins subject to intense x-irradiation [61,62]. It involves reaction of the aldehydic group of the glutaraldehyde with ε-amino groups in the protein sidechains, usually Lys. The Schiff base linkage that is formed yields cross-linked protein monomers and a "polymerized protein crystal". A protein that has been studied extensively with crosslinking is lysozyme, and accordingly we choose ^{15}N labelled hen egg-white lysozyme (^{15}N-HEWL) for a preliminary investigation of this approach.

Crystallization and crosslinking of ^{15}N-HEWL was performed using established protocols [62,63] (See Section 17 of the supplementary material for a more detailed description). The formation of the Schiff base linkages is confirmed by the spectra in Fig. 11 where the top trace shows the ^{15}N spectrum of lysozyme crystals

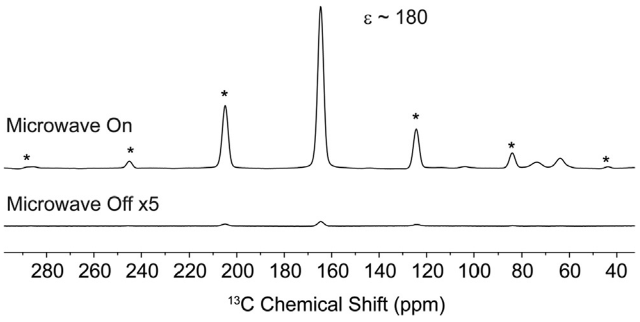

Fig. 10. DNP enhanced ^{13}C CPMAS spectra of 1 M uniformly ^{13}C labelled urea in 60:30:10 (w/w) glycerol-d_8:D_2O:H_2O with and without microwave irradiation. The spectra were recorded using a 3.2 mm sapphire rotor at a MAS rate of 5 kHz at 77 K. The sample contained 8.85 mM AMUPol as the polarizing agent and the estimated μw power at the sample is 9.1 W.

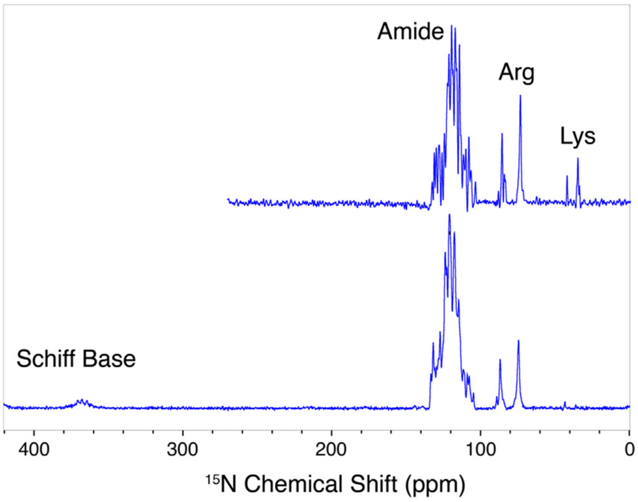

Fig. 11. (*top*) 800 MHz MAS spectrum recorded at $\omega_r/2\pi = 20$ kHz of ^{15}N label hen egg white lysozyme (^{15}N-HEWL) exhibiting he expected lines from the amide (120–130 ppm), Arg (~80 ppm) and Lys ((~40 ppm). (*bottom*) 800 MHz MAS spectrum obtained from cross-linked ^{15}N-HEWL illustrating that the Lys lines are gone and replaced by Schiff base at 360–380 ppm.

and the expected lines from the amide, Arg and Lys ^{15}N's. The single His in lysozyme is not observed in the spectrum perhaps because of chemical exchange broadening. The bottom trace of Fig. 11 was recorded following reaction with glutaraldehyde, and the Lys lines at ~40 ppm are no longer present and are replaced by at least three Schiff base lines located in the interval 360–380 ppm as expected [64,65] confirming the presence of cross linked protein. The increased linewidth is likely due to the fact that the cross-linking slows the backbone dynamics into a regime where it interferes with the ^{1}H decoupling. More detailed studies are underway to investigate this phemomenon.

Following the cross linking the ^{15}N-XL-HEWL crystals were equilibrated in DNP juice containing 10 mM AMUPol for two hours before packing into a 3.2 mm sapphire rotor. Visual inspection of the crystals indicated that they were insoluble in DNP-juice, and the DNP experiment at 500 MHz, $\omega_r/2\pi = 8$ kHz yielded the 1D ^{15}N spectra shown in Fig. 12. We observed an on/off enhancement $\varepsilon = 115$ for ^{15}N signals from backbone amides which is the most prominent signal in the spectrum. In addition we observe signals from the Arg sidechains, and probably the single His in HEWL [66] and probably some residual lysines. We do not observe intensity in the 370 ppm region expected for the Schiff base. The ^{13}C enhancement for the solvent glycerol is $\varepsilon = 180$ and larger than that for the protein, and this differential enhancement is typical for heterogeneous systems [59,60] and indicates that the radical is not in close proximity to the target protein. The attenuated enhancement may be due to dynamics of the protein.

A comparison of the ^{15}N spectra in Figs. 11 and 12 shows that the resolution is lower at ~90 K, as has been observed previously. In at least two cases it appears that this decrease is at least partially due to homogeneous broadening [23,67] and this problem can be addressed by spinning faster, going to higher fields and/or decoupling with larger Rabi fields. These are options that we are currently exploring and will report on in a future publication. In the meantime, we have used ^{15}N-^{13}C TEDOR spectra to establish that the resolution is reasonably high. Note that while the crosslinked HEWL sample is ^{15}N labelled, it is natural abundance in ^{13}C, but the sensitivity available from DNP permitted us to record a ^{15}N-^{13}C ZF TEDOR spectrum with excellent signal to noise and establish that resolution in some of the individual cross peaks is <1 ppm. The ^{15}N-^{13}C TEDOR spectrum is illustrated in in Fig. 13, and the observed ^{13}C = O linewidths for the cross peaks at $\delta_{(^{15}\mathrm{N},^{13}\mathrm{C})}$ are (111.3,179.8), (111.2, 178.2) and (110.9,176.9) ppm are 95.9, 94.1 and 95.6 Hz respectively, while in the ^{15}N dimension they are 75, 89, and 90 Hz . Thus, in the ^{13}C dimensions the linewidths are <1 ppm, and in the ^{15}N dimension <2 ppm. With the incorporation of J-decoupling into the experiment, the linewidths could improve further. Thus, cross-linked lysozyme could prove to be an ideal sample to develop new approaches for performing MAS DNP experiments.

As a second illustration of the performance of our probe and spectrometer we examined some experiments on a biologically relevant RNA Riboswitch-Aptamer. RNA's are important biomolecules controlling and regulating various cellular processes including gene expression and protein synthesis. Knowledge about the 3D structure is necessary to understand their role in biological processes. The secondary and tertiary structure of an RNA is mainly stabilized via hydrogen bonding between base pairs. Homo and heteronuclear dipolar correlation experiments are shown to be useful in the identification of base pairing and structural characterization of RNA and RNA-protein complexes [66,67]. DNP helps to

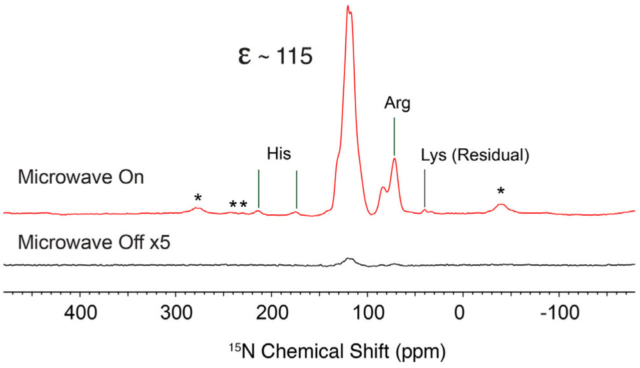

Fig. 12. DNP enhanced ^{15}N CP MAS spectra of uniformly ^{15}N labelled cross-linked hen egg white lysozyme (HEWL) equilibrated in 60:30:10 (w/w/w) glycerol-d$_8$: D$_2$O:H$_2$O solvent containing 10 mM AMUPol. The spectra were recorded using a 3.2 mm sapphire rotor at a $\omega_r/2\pi = 8$ kHz and the estimated μw power at the sample is 9.1 W. Top trace: Microwave on, 94.5 K, 32 scans; Bottom Trace: Microwave off: 91.5 K, 256 scans. The asterisk denote the position of rotational sidebands.

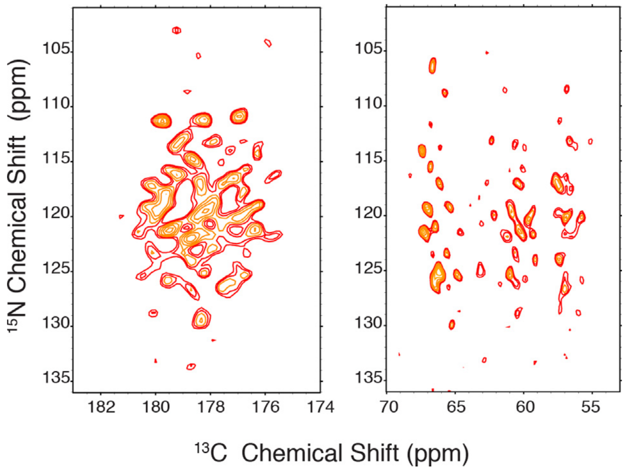

Fig. 13. DNP enhanced TEDOR spectra of natural abundance ^{13}C, uniformly ^{15}N labelled cross-linked HEWL, dissolved in 60:30:10 (w/w) glycerol-d$_8$: D$_2$O:H$_2$O with 10 mM AMUPol at 124 K. Left: Carbonyl region, Right: Cα region. The spectrum was recorded with 2.2 ms ^{13}C-^{15}N mixing. Other experimental parameters are: 128 evolution increments with 192 scans each, recycle delay 4 s, 83 kHz TPPM decoupling, 136 μs evolution increment, continuous μw irradiation (9.1 W).

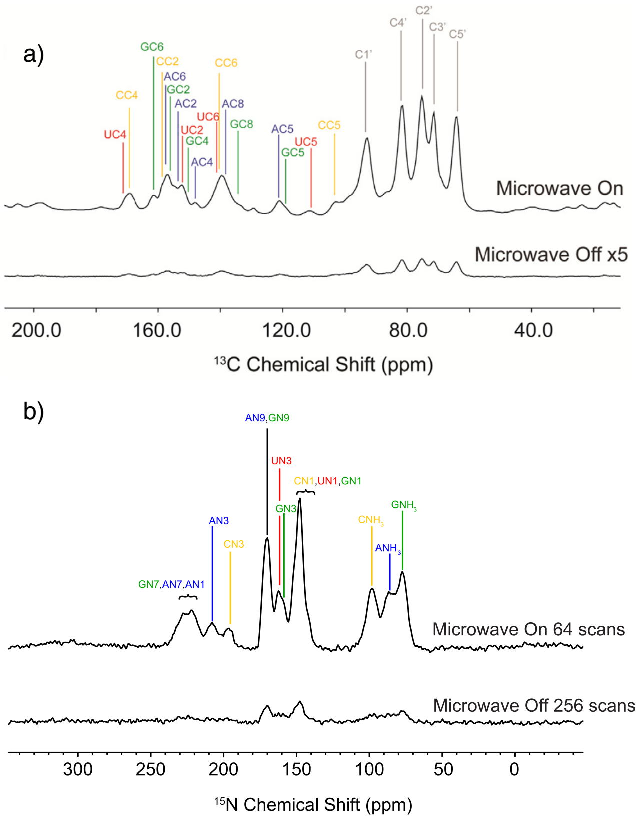

Fig. 14. (a) ^{13}C, (b)^{15}N CP MAS spectra of uniformly ^{13}C/^{15}N labelled 2′dG-sensing 70-mer RNA, 4 mg, dissolved in 60:30:10 (w/w) glycerol-d8:D_2O:H_2O with and without microwave irradiation. The spectra were recorded using a 3.2 mm Zirconia rotor at a MAS rate of 6.4 kHz. Assignments were done according to Wenk et al. [70]. An enhancement of 30 was observed for both ^{13}C and ^{15}N at 92.6 K. The sample contained 5 mM AMUPol as the polarizing agent and the estimated µw power at the sample is 2.1 W.

perform these experiments with much better sensitivity. A few examples of DNP-enhancements in studies of nucleic acids have already been reported [68].

Fig. 14 shows the enhancements obtained with uniformly ^{13}C/^{15}N labelled 2′dG-sensing 70-mer RNA sample with 2.1 W microwave irradiation.. Significant enhancements could be achieved even with low power microwave irradiation. Further we have performed a DNP enhanced two dimensional z-filtered TEDOR experiment on this sample. With the help of DNP, we could observe all the expected intramolecular cross peaks within in a very short experimental time of two and a half hours (Fig. 15).

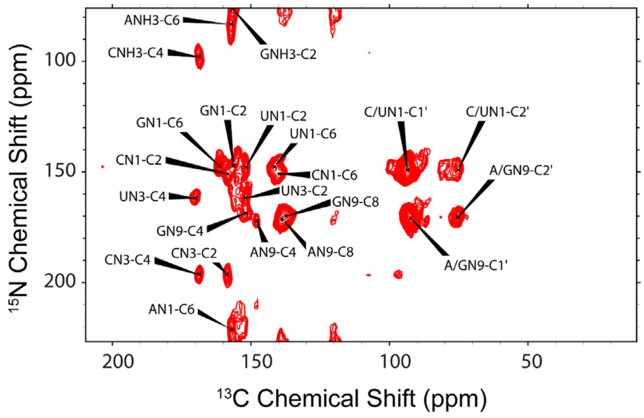

Fig. 15. DNP enhanced TEDOR spectra of uniformly ^{13}C/^{15}N labelled 2′dG-sensing 70-mer RNA, 4 mg, dissolved in 60:30:10 (w/w) glycerol-d8: D_2O:H_2O at 93 K. The spectrum was recorded in 2 h 20 min. with 2 ms ^{13}C-^{15}N mixing. Other experimental parameters are: 64 evolution increments with 16 scans each, recycle delay 4 s, 83 kHz TPPM decoupling, 129 µs evolution increment, continuous µw irradiation (2.1 W).

In summary our balanced transmission line probe shows excellent DNP performance at cryogenic temperatures. Magic angle spinning up to 8.5 kHz is possible at 80 K.

8. Conclusions

In summary we have presented in detail a novel design, construction and characterization strategy for a fully balanced ^{1}H/^{13}C/^{15}N triple resonance transmission line probe, and demonstrated its function on samples of cross-linked lysozyme and RNA. A second version of the probe utilizing the identical design and construction principles for ^{1}H/^{31}P/^{15}N is almost complete and exhibits similar operational characteristics. Both probes function with a 500 MHz/330 GHz DNP gyrotron.

Our aim was to achieve high RF field strengths, optimal sensitivity and RF homogeneity and high duty cycle on all three channels. The novel design and characterization strategy employed permitted us to achieve this goal. This strategy included both electromagnetic simulations as well as experimental verification. By designing the probe with swappable modules, interconnected with common transmission line ports, each probe component could be characterized independently. A set of four transmission line adapters were designed to mate with these ports at one end and a standard type-N port at the other. To facilitate the balancing of the RF coil simultaneously at all three channels, the probe was made symmetric with respect to its mid plane. Further a stepped transmission line inner conductor was designed to generate impedance minima at the four-way tee for all the design frequencies. Accurate impedance measurements at the tee ensured good isolation between the channels without employing any traps. The RF performance of the probe was excellent with the carbon channel reaching a Rabi frequency of 280 KHz.

The probe is integrated into a 330 GHz/500 MHz DNP NMR spectrometer and gives excellent DNP performance as well. An enhancement factor ε = 180 was achieved for U-^{13}C urea in the glassy matrix doped with 9 mM AMUPol at 77 K and with 9.1 W microwave irradiation at the sample and ε = 115 on cross-linked lysozyme and RNA samples.

Acknowledgements

This research was supported by the National Institute of General Medical Sciences (GM132997 and GM132079) and the National Institute of Biomedical Imaging and Bioengineering (EB001965 and EB004866). Thanks are accorded to Ajay Thakkar and Michael Mullins (Francis Bitter Magnet Laboratory) as well as to Andrew J Gallant and his team, in particular Michael Abruzzese, Chris Freeman, Stephen Galinos, Ernie Johnson and Scott Spence (all MIT Central Machine Shop) for their invaluable technical assistance.

Appendix A. Supplementary material

Supplementary data to this article can be found online at https://doi.org/10.1016/j.jmr.2019.106573.

References

[1] L.R. Becerra, G.J. Gerfen, R.J. Temkin, D.J. Singel, R.G. Griffin, Dynamic nuclear polarization with a cyclotron resonance maser at 5 T, Phys. Rev. Lett. 71 (1993) 3561–3564.

[2] G.J. Gerfen, L.R. Becerra, D.A. Hall, R.G. Griffin, R.J. Temkin, D.J. Singel, High-frequency (140 GHz) dynamic nuclear-polarization - polarization transfer to a solute in frozen aqueous-solution, J. Chem. Phys. 102 (1995) 9494–9497.

[3] D.A. Hall, D.C. Maus, G.J. Gerfen, S.J. Inati, L.R. Becerra, F.W. Dahlquist, R.G. Griffin, Polarization-enhanced NMR spectroscopy of biomolecules in frozen solution, Science 276 (1997) 930–932.

[4] Q.Z. Ni, E. Daviso, T.V. Can, E. Markhasin, S.K. Jawla, T.M. Swager, R.J. Temkin, J. Herzfeld, R.G. Griffin, High frequency dynamic nuclear polarization, Acc Chem Res 46 (2013) 1933–1941.

[5] D. Lee, E. Bouleau, P. Saint-Bonnet, S. Hediger, G. De Paepe, Ultra-low temperature MAS-DNP, J. Magn. Reson. 264 (2016) 116–124.

[6] K.-N. Hu, C. Song, H.-H. Yu, T.M. Swager, R.G. Griffin, High-frequency dynamic nuclear polarization using biradicals: a multifrequency EPR lineshape analysis, J. Chem. Phys. 128 (2008) 052321.

[7] C.S. Song, K.N. Hu, C.G. Joo, T.M. Swager, R.G. Griffin, TOTAPOL: A biradical polarizing agent for dynamic nuclear polarization experiments in aqueous media, J. Am. Chem. Soc. 128 (2006) 11385–11390.

[8] D.J. Kubicki, G. Casano, M. Schwarzwalder, S. Abel, C. Sauvee, K. Ganesan, M. Yulikov, A.J. Rossini, G. Jeschke, C. Coperet, A. Lesage, P. Tordo, O. Ouari, L. Emsley, Rational design of dinitroxide biradicals for efficient cross-effect dynamic nuclear polarization, Chem. Sci. 7 (2016) 550–558.

[9] C. Sauvee, M. Rosay, G. Casano, F. Aussenac, R.T. Weber, O. Ouari, P. Tordo, Highly efficient, water-soluble polarizing agents for dynamic nuclear polarization at high frequency, Angewandte Chemie-Int. Ed. 52 (2013) 10858–10861.

[10] G. Mathies, M.A. Caporini, V.K. Michaelis, Y.P. Liu, K.N. Hu, D. Mance, J.L. Zweier, M. Rosay, M. Baldus, R.G. Griffin, Efficient dynamic nuclear polarization at 800 MHz/527 GHz with trityl-nitroxide biradicals, Angewandte Chemie-Int. Ed. 54 (2015) 11770–11774.

[11] D.P. Raleigh, M.H. Levitt, R.G. Griffin, Rotational resonance in solid state NMR, Chem. Phys. Lett. 146 (1988) 71–76.

[12] D.P. Raleigh, F. Creuzet, S.K.D. Gupta, M.H. Levitt, R.G. Griffin, Measurement of internuclear distances in polycrystalline solids - rotationally enhanced transfer of nuclear-spin magnetization, J. Am. Chem. Soc. 111 (1989) 4502–4503.

[13] J.M. Griffiths, R.G. Griffin, Nuclear-magnetic-resonance methods for measuring dipolar couplings in rotating solids, Anal. Chim. Acta 283 (1993) 1081–1101.

[14] A.E. Bennett, J.H. Ok, R.G. Griffin, S. Vega, Chemical-shift correlation spectroscopy in rotating solids - radio frequency-driven dipolar recoupling and longitudinal exchange, J. Chem. Phys. 96 (1992) 8624–8627.

[15] A.E. Bennett, L.R. Becerra, R.G. Griffin, Frequency-selective heteronuclear recoupling in rotating solids, J. Chem. Phys. 100 (1994) 812–814.

[16] A.E. Bennett, R.G. Griffin, S. Vega, Recoupling of homo- and heteronuclear dipolar interactions in rotating solids, NMR Basic Principles Progr. 33 (1994) 1–77.

[17] J.M. Griffiths, K.V. Lakshmi, A.E. Bennett, J. Raap, C.M. Vanderwielen, J. Lugtenburg, J. Herzfeld, R.G. Griffin, Dipolar correlation NMR-spectroscopy of a membrane-protein, J. Am. Chem. Soc. 116 (1994) 10178–10181.

[18] V.S. Bajaj, M.L. Mak-Jurkauskas, M. Belenky, J. Herzfeld, R.G. Griffin, DNP enhanced frequency-selective TEDOR experiments in bacteriorhodopsin, J. Mag. Reson. 202 (2010) 9–13.

[19] V.S. Bajaj, M.L. Mak-Jurkauskas, M. Belenky, J. Herzfeld, R.G. Griffin, Functional and shunt states of bacteriorhodopsin resolved by 250-GHz dynamic nuclear polarization-enhanced solid-state NMR Proc, Nat'l. Acad. Sci. 106 (2009) 9244–9249.

[20] Q.Z. Ni, T.V. Can, E. Daviso, M. Belenky, R.G. Griffin, J. Herzfeld, Primary transfer step in the light-driven ion pump bacteriorhodopsin: an irreversible U-turn revealed by dynamic nuclear polarization-enhanced magic angle spinning NMR, J. Am. Chem. Soc. 140 (2018) 4085–4091.

[21] U. Akbey, W.T. Franks, A. Linden, S. Lange, R.G. Griffin, B.J. van Rossum, H. Oschkinat, Dynamic nuclear polarization of deuterated proteins, Angew. Chem. Int. Ed. Engl. 49 (2010) 7803–7806.

[22] F. Mentink-Vigier, U. Akbey, H. Oschkinat, S. Vega, A. Feintuch, Theoretical aspects of Magic Angle Spinning - Dynamic Nuclear Polarization, J. Magn. Reson. 258 (2015) 102–120.

[23] K. Jaudzems, A. Bertarello, S.R. Chaudhari, A. Pica, D. Cala-De Paepe, E. Barbet-Massin, A.J. Pell, I. Akopjana, S. Kotelovica, D. Gajan, O. Ouari, K. Tars, G. Pintacuda, A. Lesage, Dynamic nuclear polarization-enhanced biomolecular NMR spectroscopy at high magnetic field with fast magic-angle spinning, Angewandte Chemie (International ed. in English) 57 (2018) 7458–7462.

[24] K. Jaudzems, T. Polenova, G. Pintacuda, H. Oschkinat, A. Lesage, DNP NMR of biomolecular assemblies, J. Struct. Biol. 206 (2019) 90–98.

[25] V. Weis, M. Bennati, M. Rosay, J.A. Bryant, R.G. Griffin, High-field DNP and ENDOR with a novel multiple-frequency resonance structure, J. Magn. Reson. 140 (1999) 293–299.

[26] V.S. Bajaj, C.T. Farrar, M.K. Hornstein, I. Mastovsky, J. Vieregg, J. Bryant, B. Elena, K.E. Kreischer, R.J. Temkin, R.G. Griffin, Dynamic nuclear polarization at 9T using a novel 250 GHz gyrotron microwave source, J. Mag. Res. 160 (2003) 85–90.

[27] A.B. Barnes, E. Markhasin, E. Daviso, V.K. Michaelis, E.A. Nanni, S. Jawla, E. Mena, R. DeRocher, A. Thakkar, P. Woskow, R.J.T.J. Herzfeld, R.G. Griffin, Dynamic nuclear polarization at 700 MHz/460 GHz, J. Magn. Reson. 221 (2012) 1–7.

[28] A.B. Barnes, M.L. Mak-Jurkauskas, Y. Matsuki, V.S. Bajaj, P.C. van der Wel, R. Derocher, J. Bryant, J.R. Sirigiri, R.J. Temkin, J. Lugtenburg, J. Herzfeld, R.G. Griffin, Cryogenic sample exchange NMR probe for magic angle spinning dynamic nuclear polarization, J. Magn. Reson. 198 (2009) 261–270.

[29] A.A. Smith, B. Corzilius, J.A. Bryant, R. DeRocher, P.P. Woskov, R.J. Temkin, R.G. Griffin, A 140 GHz pulsed EPR/212 MHz NMR spectrometer for DNP studies, J. Magn. Reson. 223 (2012) 170–179.

[30] E. Bouleau, P. Saint-Bonnet, F. Mentink-Vigier, H. Takahashi, J.F. Jacquot, M. Bardet, F. Aussenac, A. Purea, F. Engelke, S. Hediger, D. Lee, G. De Paepe, Pushing NMR sensitivity limits using dynamic nuclear polarization with closed-loop cryogenic helium sample spinning, Chem. Sci. 6 (2015) 6806–6812.

[31] A. Purea, C. Reiter, A.I. Dimitriadis, E. de Rijk, F. Aussenac, I. Sergeyev, M. Rosay, F. Engelke, Improved waveguide coupling for 1.3 mm MAS DNP probes at 263 GHz, J. Magn. Reson. 302 (2019) 43–49.

[32] M. Rosay, M. Blank, F. Engelke, Instrumentation for solid-state dynamic nuclear polarization with magic angle spinning NMR, J. Magn. Reson. 264 (2016) 88–98.

[33] K. Thurber, R. Tycko, Low-temperature dynamic nuclear polarization with helium-cooled samples and nitrogen-driven magic-angle spinning, J. Magn. Reson. 264 (2016) 99–106.

[34] Y. Matsuki, T. Idehara, J. Fukazawa, T. Fujiwara, Advanced instrumentation for DNP-enhanced MAS NMR for higher magnetic fields and lower temperatures, J. Magn. Reson. 264 (2016) 107–115.

[35] C.S. Yannoni, P.C. Myhre, G.G. Webb, Magic angle spinning nuclear magnetic resonance near liquid-helium temperatures. Variable-temperature CPMAS spectra of the 2-norbornyl cation to 6 K, J. Am. Chem. Soc. 112 (1990) 8991–8992.

[36] A. Hackmann, H. Seidel, R.D. Kendrick, P.C. Myhre, C.S. Yannoni, Magic-angle spinning NMR at near-liquid-helium temperatures, J. Magn. Reson. 79 (1988) 148–153.

[37] M. Concistre, O.G. Johannessen, E. Carignani, M. Geppi, M.H. Levitt, Magic-angle spinning NMR of cold samples, Acc. Chem. Res. (2013) Ahead of Print.

[38] A. Samoson, I. Heinmaa, T. Tuherm, A. Reinhold, J. Past, R. Stern, T. Anupold, A high resolution low temperature solid-state nuclear magnetic resonance probe, in: (Keemilise Ja Bioloogilise Fueuesika Instituut (The National Institute of Chemical Physics and Biophysics), Estonia). Application: WO, 2005, pp. 7 pp.

[39] E.A. Nanni, A.B. Barnes, R.G. Griffin, R.J. Temkin, THz Dynamic Nuclear Polarization NMR, IEEE Trans. Terahertz Sci. Technol. 1 (2011) 145–163.

[40] A.C. Torrezan, M.A. Shapiro, J.R. Sirigiri, R.J. Temkin, R.G. Griffin, Operation of a continuously frequency-tunable second-harmonic CW 330-GHz gyrotron for dynamic nuclear polarization, IEEE Trans. Electron Devices 58 (2011) 2777–2783.

[41] P.W. Woskov, V.S. Bajaj, M.K. Hornstein, R.J. Temkin, R.G. Griffin, Corrugated waveguide and directional coupler for CW 250 GHz gyrotron DNP experiments, IEEE Trans. Microw. Theory Tech. 53 (2005) 1863–1869.

[42] A.B. Barnes, E.A. Nanni, J. Herzfeld, R.G. Griffin, R.J. Temkin, A 250 GHz gyrotron with a 3 GHz tuning bandwidth for dynamic nuclear polarization, J. Magn. Reson. 221 (2012) 147–153.

[43] M. Rosay, L. Tometich, S. Pawsey, R. Bader, R. Schauwecker, M. Blank, P.M. Borchard, S.R. Cauffman, K.L. Felch, R.T. Weber, R.J. Temkin, R.G. Griffin, W.E. Maas, Solid-state dynamic nuclear polarization at 263 GHz: spectrometer design and experimental results, Phys. Chem. Chem. Phys. 12 (2010) 5850–5860.

[44] J. Schaefer, R.A. McKay, Multituned Single Coil Transmission Line Probe for Nuclear Magnetic Resonance Spectrometer (US Patent # 5,861,748), in: United States, 1999.

[45] V.R. Cross, R.K. Hester, J.S. Waugh, Single Coil Probe with Transmission-Line Tuning for Nuclear Magnetic Double Resonance, Rev. Sci. Instrum. 47 (1976) 1486–1488.

[46] J.A. Frydel, M. Krzystyniak, D. Pienkowski, M. Pietrzak, N.D. Amadeu, T. Ratajczyk, K. Idzik, T. Gutmann, D. Tietze, S. Voigt, A. Fenn, H.H. Limbach, G. Buntkowsky, Efficient design of multituned transmission line NMR probes: The electrical engineering approach, Solid State Nucl. Mag. 39 (2011) 72–80.

[47] C.Q. Qian, W.W. Brey, Impedance matching with an adjustable segmented transmission line, J. Magn. Reson. 199 (2009) 104–110.

[48] E.K. Paulson, R.W. Martin, K.W. Zilm, Cross polarization, radio frequency field homogeneity, and circuit balancing in high field solid state NMR probes, J. Magn. Reson. 171 (2004) 314.

[49] F. Engelke, Electromagnetic wave compression and radio frequency homogeneity in NMR solenoidal coils: Computational approach, Concepts Magn. Reson. 15 (2002) 129.

[50] E. Markhasin, J. Hu, Y. Su, J. Herzfeld, R.G. Griffin, Efficient, balanced, transmission line RF circuits by back propagation of common impedance nodes, J. Magn. Reson. 231 (2013) 32–38.

[51] R.W. Martin, E.K. Paulson, K.W. Zilm, Design of a triple resonance magic angle sample spinning probe for high field solid state nuclear magnetic resonance, Rev. Sci. Instrum. 74 (2003) 3045–3061.

[52] K.A. Collier, S. Sengupta, C.A. Espinosa, J.E. Kelly, J.I. Kelz, R.W. Martin, Design and construction of a quadruple-resonance MAS NMR probe for investigation of extensively deuterated biomolecules, J. Magn. Reson. 285 (2017) 8–17.

[53] S.J. Orfanidis, Electromagnetic Waves and Antennas, Rutgers University, https://www.ece.rutgers.edu/~orfanidi/ewa, 2016.

[54] E.A. Nanni, A.B. Barnes, Y. Matsuki, P.P. Woskov, B. Corzilius, R.G. Griffin, R.J. Temkin, Microwave field distribution in a magic angle spinning dynamic nuclear polarization NMR probe, J. Magn. Reson. 210 (2011) 16–23.

[55] E.A. Nanni, S.K. Jawla, M.A. Shapiro, P.P. Woskov, R.J. Temkin, Low-loss Transmission Lines for High-power Terahertz Radiation, J. Infrared Millim. Terahertz Waves 33 (2012) 695–714.

[56] A. Wacker, J. Buck, D. Mathieu, C. Richter, J. Wohnert, H. Schwalbe, Structure and dynamics of the deoxyguanosine-sensing riboswitch studied by NMR-spectroscopy, Nucleic Acids Res. 39 (2011) 6802–6812.

[57] W.T. Franks, D.H. Zhou, B.J. Wylie, B.G. Money, D.T. Graesser, H.L. Frericks, G. Sahota, C.M. Rienstra, Magic-angle spinning solid-state NMR spectroscopy of the beta 1 immunoglobulin binding domain of protein G (GB1): N-15 and C-13 chemical shift assignments and conformational analysis, J. Am. Chem. Soc. 127 (2005) 12291–12305.

[58] P.C. van der Wel, M.T. Eddy, R. Ramachandran, R.G. Griffin, Targeted 13C–13C distance measurements in a microcrystalline protein via J-decoupled rotational resonance width measurements, ChemPhysChem 10 (2009) 1656–1663.

[59] P.C.A. van der Wel, K.N. Hu, J. Lewandowski, R.G. Griffin, Dynamic nuclear polarization of amyloidogenic peptide nanocrystals: GNNQQNY, a core segment of the yeast prion protein Sup35p, J. Am. Chem. Soc. 128 (2006) 10840–10846.

[60] G.T. Debelouchina, M.J. Bayro, P.C.A.V.D. Wel, M.A. Caporini, A.B. Barnes, M. Rosay, W.E. Maas, R.G. Griffin, Dynamic nuclear polarization-enhanced solid-state NMR spectroscopy of GNNQQNY nanocrystals and amyloid fibrils, Phys. Chem. Chem. Phys. 12 (2010).

[61] I. Migneault, C. Dartiguenave, M.J. Bertrand, K.C. Waldron, Glutaraldehyde: behavior in aqueous solution, reaction with proteins, and application to enzyme crosslinking, Biotechniques 37 (2004) 790-+.

[62] Y. Wine, N. Cohen-Hadar, A. Freeman, F. Frolow, Elucidation of the mechanism and end products of glutaraldehyde crosslinking reaction by X-ray structure analysis, Biotechnol. Bioeng. 98 (2007) 711–718.

[63] R.W. Martin, K.W. Zilm, Preparation of protein nanocrystals and their characterization by solid state NMR, J. Magn. Reson. 164 (2003) 162–174.

[64] G.S. Harbison, J. Herzfeld, R.G. Griffin, Solid-State ^{15}N Nuclear Magnetic-Resonance Study of the Schiff-Base in Bacteriorhodopsin, Biochemistry 22 (1983) 1–5.

[65] H.J. de Groot, G.S. Harbison, J. Herzfeld, R.G. Griffin, Nuclear magnetic resonance study of the Schiff base in bacteriorhodopsin: counterion effects on the 15N shift anisotropy, Biochemistry 28 (1989) 3346–3353.

[66] M. Munowitz, W.W. Bachovchin, J. Herzfeld, C.M. Dobson, R.G. Griffin, Acid-Base and Tautomeric Equilibria in the Solid State: 15N NMR Spectroscopy of Histidine and Imidazole, J. Am. Chem. Soc. 104 (1982) 1192–1196.

[67] P. Fricke, D. Mance, V. Chevelkov, K. Giller, S. Becker, M. Baldus, A. Lange, High resolution observed in 800 MHz DNP spectra of extremely rigid type III secretion needles, J. Biomol. NMR 65 (2016) 121–126.

[68] V. Aladin, M. Vogel, R. Binder, I. Burghardt, B. Suess, B. Corzilius, Complex formation of the tetracycline-binding aptamer investigated by specific cross-relaxation under DNP, Angewandte Chemie-Int. Ed. 58 (2019) 4863–4868.